Penetration Mechanics of GLARE™ Fiber-Metal Laminates upon Collision with Micrometeoroids

Md. Zahid Hasan[1]

Abstract

The spacecraft designed for long-duration service are susceptible to hypervelocity impacts of micrometeoroids and orbiting space debris. Such impacts on spacecraft structures can cause spacecraft failure and loss of life. In order to adequately protect the spacecraft bulkhead and flight critical systems, many high-strength composite materials have been developed for debris bumper. GLAss fiber REinforced aluminum is one of the high-performance composites. The review of articles, however, yielded no single study, which has been dedicated to interrogate the damage mechanics of GLAss fiber REinforced aluminum upon collision with micrometeoroids. This study, therefore, aimed at the numerical investigation of penetration phenomena of thick GLAss fiber REinforced aluminum 5-6/5-0.4 laminates upon hypervelocity impact of a projectile. The numerical study employed a predictive model that merged the smoothed particle hydrodynamics and the finite element methods. The model could predict the colossal damage modes of GLAss fiber REinforced aluminum. As seen, the normal impact of a 2 mm diameter spherical 2024-T3 aluminum projectile on GLAss fiber REinforced aluminum, at a relative velocity of 7.11 km/s, resulted into membrane stretching and fiber failure of the glass fiber reinforced epoxy composite laminates. By contrast, the aluminum layers experienced an enormous strain-rate and consequently, suffered thinning, fracture and large mass erosion. The perpetual release waves fragmented the projectile and dispersed the projectile mass prior to the further penetration of GLAss fiber REinforced aluminum. To verify the accuracy of the numerical model, experiments had been conducted by using a two-stage light-gas gun. The experiments generated damage modes of GLAss fiber REinforced aluminum in good correspondence to that of the predictive model. Yet, disparity between the estimations of experiments and simulations had been apparent, which is anticipated due to the phase change of material had not been accounted for in the analysis.

Abbreviations

Al	Aluminum
ALE	Arbitrary–Lagrangian–Eulerian
CFL	Courant–Friedrichs–Lewy
EOS	Equation of state
FEM	Finite element method
FMLs	Fiber metal laminates
FTIS	Forward time integration scheme
GF/EP	Glass fiber reinforced epoxy
GF/PP	Glass fiber reinforced polypropylene
GLARE	GLAss fiber reinforced aluminum
HEL	Hugoniot elastic limit
HVI	Hypervelocity impact
ISS	International space station
SPH	Smoothed particle hydrodynamics

✉ Md. Zahid Hasan
 md.zahidhasan83@yahoo.de

1 Designing Plastics and Composite Materials Department, Montan University, Otto Gloeckel Street 2, 8700 Leoben, Austria

Introduction

Impact Shields

Of the many shockwave-accompanied fragmentation phenomena, the astrophysical event that reigns supreme is the creation of the visible Universe. The 'Big Bang' released enormous energy that led to the expansion of many galaxies. If the characteristic length scale is adequately large, the Universe is expected to be isotropic and undergo uniform expansion. The underlying physics of the zero origin and

subsequent inflation of the Universe can be extrapolated to lend insights in the shockwave-engendered fragmentation process of advanced engineering materials. However, the engineering materials in spacecraft applications have evolved to be orthotropic to perform in unpredictable loading conditions of the hostile space environment.

Orthotropic fiber-reinforced composite materials have been used in the primary shielding system of manned spacecraft, for example, the International Space Station (ISS) [1]. The hypervelocity impact-induced damage of a composite protection shield appears in dissimilar modes, to name a few, transverse micro-cracking, punch shear, delamination, fiber breakage, and spallation [2, 3]. The harsh space environment makes the inflicted damage grow at a distressing rate. A GLAss fiber REinforced aluminum (GLARE) protection shield, by contrast, favors the structural integrity. Because, GLARE promotes the crack bridging mechanism through multiple load paths, attributed to its alternate metal/composite stacking sequence [4]. Furthermore, GLARE combines the synergistic advantages of high energy dissipation in the isotropic monolithic thin aluminum (Al 2024-T3) sheets and appreciable strength of orthotropic S2-glass/FM94-epoxy (GF/EP) composite [5, 6]. A detailed interrogation of GLARE damage modes under cataclysmic strain-rates, yet, is imperative. By analyzing the damage modes, the material layers prone to exacerbated damage can be demarcated and improved in order to optimize their mechanical properties and make the GLARE stack fit for future spacecraft applications. The main objective of this study, therefore, was to understand the physics of penetration mechanism of GLARE through numerical analysis. Because, the hypervelocity impact experiments elucidate the damaged state of a composite panel, but do not delineate the temporal evolution of damage in the interior of a solid domain. Besides, this study analyzed the wave release at the free surface of GLARE, which leads to the decompression and the fragmentation of material following the shockwave-induced compression. Doing so, the shockwave dissipation and the damage-prone material layers could be determined. The GLARE damage helped identify the critical design parameters, which were upgraded to propose a potential GLARE candidate for spacecraft structures.

Existing Numerical Models

Concomitant with many experimental studies on the impact behavior of GLARE [7, 8] countable numerical investigations have been made available for public release to partially replace the experimental characterization of fiber-metal laminates (FMLs). Sitnikova et al. [9] employed: a three dimensional (3D) progressive damage model for woven glass-fiber reinforced polypropylene (GF/PP) composite, the Johnson–Cook plasticity model for Al-alloy sheets, and

cohesive zones between these mating material layers. The model could reproduce blast failure modes of the test specimens exemplified in Ref. [10]. The incorporation of instantaneous failure of ceased elements, even though, underestimated the load-carrying ability of GF/PP.

Next, Guan et al. [11] further extended the 3D progressive damage model by using strain-rate dependent plasticity for the Al-alloy of Al-PP/PP 0°/90° 2/1 and 5/4. The model predicted a higher permanent displacement of 2/1 grades compared to that of the 5/4 grades for impact velocities up to 150 m/s. The 5/4 grades suffered significant tensile fractures. Rough contacts between the mating layers allowed no debonding or delamination. By comparison, the FEM model of Karagiozova et al. [12] accommodated cohesive zones in the Al-GF/PP interfaces to reconstruct debonding. The model confirmed the dependency of laminate transverse velocity on the through-thickness properties of GF/PP, although, ignored the damage of GF/PP continua.

In place of a discrete cohesive zone approach, Yaghoubi et al. [13] opted for surface-to-surface contacts between Al layers and GF/EP composite laminates. Their model could predict the ballistic limit of GLARE 5-3/2 beams and reconstruct plastic hinging and thinning of the outer Al-skins. An erosion scheme, when met the strain-based failure criteria, removed the torn fibers from the computational domain. In a complementary study, Fan et al. [14] proposed a numerical model by using the framework outlined by Guan et al. [11]. For low velocity impacts, the model exhibited fiber fracture of GF/EP and plastic deformation of Al around the perforation zone of FMLs 2/1 and 4/3, in accordance with the experiments.

Next Quantum Leap

The aforementioned numerical models offer upgrades, yet, have limitations, entail assumptions and not been validated for HVI events. HVI involves an extreme plastic compression of materials, due to a rapid rise of pressure across the shockwave of high-frequency bands. To investigate the hydrostatic material compression and the shockwave-induced bulk material failure, an experimental campaign is ideal. Technical challenges and expense of experiments have ushered us in a new era of numerical models based on either a Eulerian or a Lagrangian framework, however.

In pursuit of a stable and accurate numerical model, this study adopted the Arbitrary–Lagrangian–Eulerian (ALE) framework of Autodyn-3D hydrocode to reproduce the perforation failure of a thick GLARE 5-6/5-0.4 laminate. The ALE framework accommodated single-phase non-linear equations of state, orthotropic constitutive relationships, interactive individual material plane damage initiation criteria and energy-based damage continuation criteria. The proposed model alleviated the deficiencies of stand-alone

numerical frameworks, reproduced the HVI-induced damage of GLARE, apportioned the impact energy dissipated between different failure modes and reconstructed the detailed morphology of debris clouds. Numerous failure modes were in good agreement with the experiments. The model, nevertheless, had shortcomings will be elaborated when appropriate.

Modeling Particulars

Geometry and Material

A 2 mm 2024-T3 Al-sphere impacted the front surface of the GLARE 5-6/5-0.4 target, which had an in-plane dimension of 100 mm × 100 mm and a thickness of 5 mm. The size of the fragment-simulating hydrodynamic projectile represented micrometeoroids don't leave a luminous trail in the space environment [15]. A gap interaction method specified the frictionless contact between the projectile and the GLARE target placed 0.05 mm apart. The 11.64 mg mass projectile was launched with an initial velocity at an incidence obliquity of 0° relative to the normal of the target. The 0° angle of incidence was chosen in all configurations to make sure the most transfer of projectile momentum to the target surface. The GLARE 5-6/5-0.4 laminate comprised six Al 2024-T3 layers and five S2-glass/FM94-epoxy cross-ply 0°/90°/90°/0° composite laminates. The analysis addressed only the cross-ply GLARE configuration because of its impact resistance superior to that of the other stacking sequences [4, 16]. Each Al layer and GF/EP composite laminate was respectively, 0.4 and 0.5 mm thick. A gap of 10 μm between an Al layer and a GF/EP composite laminate emulated the thickness of an inter-laminar interface, at which a surface-to-surface contact was assigned. The GLARE model had 10 pre-defined debonding interfaces. The composite laminates were represented by a homogenized orthotropic material, which eliminated the need of specifying individual GF/EP laminas in the stacking sequence. To compute the stiffness matrix constants of a GF/EP laminate, the fiber (22) direction and in-plane transverse to the fiber (33) direction of the unidirectional GF/EP lamina were aligned with the global X-axis and Y-axis, respectively. The through-thickness material direction of the GF/EP lamina followed the global Z-axis. The material properties, showed in Tables 1 and 2, were assigned to the GF/EP composite laminates and the Al sheets, respectively.

Discretization

Because of the symmetry of geometry, material properties and boundary conditions, only a quarter model of the GLARE plate and the projectile with proper symmetry and boundary conditions was constructed. A mesh-resolved FE-model demanded a change of the element size. A refined mesh smoothened the spatial derivatives. To ensure that the

Table 1 Data set of a S2-glass/FM94-epoxy (GF/EP) 0°/90°/90°/0° composite laminate

| Strength: orthotropic		Failure: orthotropic softening	
Reference density (g/cm^3)	1.8	Tensile failure stress 11 (kPa)	6.90e+004
Young's modulus 11 (kPa)	1.90e+007	Tensile failure stress 22 (kPa)	5.90e+005
Young's modulus 22 (kPa)	3.083e+007	Tensile failure stress 33 (kPa)	5.90e+005
Young's modulus 33 (kPa)	3.083e+007	Maximum shear stress 12 (kPa)	4.83e+004
Poisson's ratio 12	0.4	Maximum shear stress 23 (kPa)	8.69e+004
Poisson's ratio 23	0.114	Maximum shear stress 31 (kPa)	4.83e+004
Poisson's ratio 31	0.4	Fracture energy 11 (J/m^2)	83.375
Shear modulus 12 (kPa)	3.89e+006	Fracture energy 22 (J/m^2)	1e−006
Shear modulus 23 (kPa)	8.10e+006	Fracture energy 33 (J/m^2)	1e−006
Shear modulus 31 (kPa)	3.89e+006	Fracture energy 12 (J/m^2)	747
Reference temperature (K)	300	Fracture energy 23 (J/m^2)	1e−006
Specific heat (J/kgK)	900	Fracture energy 31 (J/m^2)	1.378e+003
Volumetric response: polynomial		Damage coupling coefficient	0.2
Bulk modulus A_1 (kPa)	2.69e+007	Erosion: failure criteria satisfied	
Parameter A_2 (kPa)	2.69e+008		
Parameter B_0	0		
Parameter B_1	0		
Parameter T_1	2.69e+007		
Parameter T_2	0		
Strength: elastic			
Shear modulus (kPa)	8.10e+006		
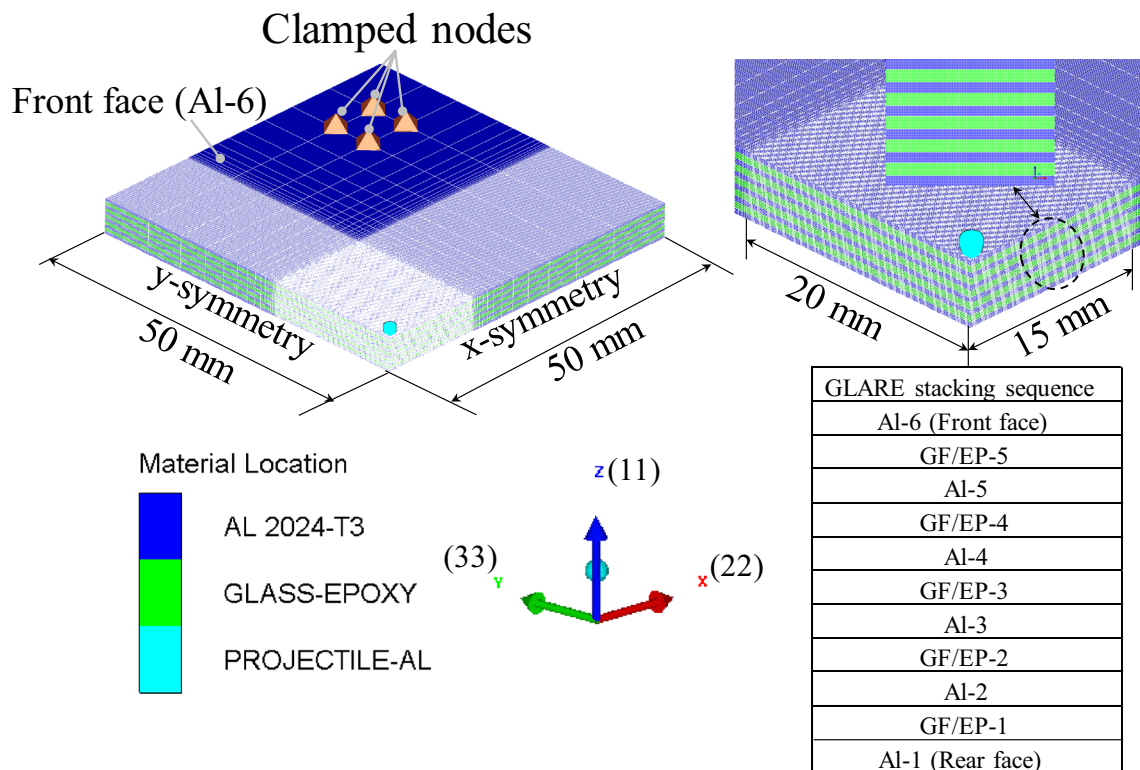
Fig. 1 Finite element (FE) model of a GLARE 5-6/5-0.4 laminate

Table 2 Data set of 2024-T3 aluminum material model [8]

Equation of state: shock		Failure: material strain	
Reference density (g/cm^3)	2.785	Tensile failure strain 11	0.225
Grüneisen coefficient	2.0	Tensile failure strain 22	0.225
Parameter C1	5.328e+003	Tensile failure strain 33	0.225
Parameter S1	1.338	Maximum shear strain 12	0.3181
Reference temperature (K)	300	Maximum shear strain 23	0.3181
Specific heat (J/kgK)	863	Maximum shear strain 31	0.3181
Strength: Steinberg Guinan		Post-failure option: isotropic	
Shear modulus (kPa)	2.86e+007	Erosion: failure criteria satisfied	For Al-sheet
Yield stress (kPa)	2.6e+005		
Maximum yield stress (kPa)	7.6e+005		
Hardening constant	310		
Hardening exponent	0.185		
Melting temperature (K)	1.22e+003		

predictions were further invariant with the mesh size, the model was finer discretized and next, compared with the one exhibited in Fig. 1. The predictions of both models collapsed on the same line in terms of kinetic- and internal energy of the target. The model, subsequently, employed the mesh given in Fig. 1. A finer mesh size of 0.1 mm × 0.1 mm circumscribed up to 15 and 20 mm in the *X*-direction and the *Y*-direction from the target center. The biased and coarser mesh toward the target's periphery reduced the computational zones and did not affect the extent of GLARE damage, since the impact damage clustered around the target center. Total 44 solid elements discretized the through-thickness direction of the GLARE plate: four elements through the thickness of an Al layer and a GF/EP composite laminate ensured a sufficient resolution.

3D full-integrated constant stress hexahedral elements were assigned to 141,900 voxels of each Al layer and GF/EP composite laminate. Smoothed particle hydrodynamics

(SPH) particles were preferred for the projectile discretization, as it is a meshless Lagrangian technique and does not entail the use of a numerical grid to compute the spatial derivatives. The particle-based framework is free of mesh-tangling and distortion usually occur in large deformation of Lagrangian elements. 1114 Lagrangian 3D SPH particles, 0.1 mm in size, populated the quarter projectile. The particle size maintained the computational accuracy at an acceptable level.

Material Models

Constitutive Equations of GF/EP

The analysis presumed the behavior of GF/EP laminates to be linear elastic until the onset of failure, related to the findings in Refs. [17, 18]. As seen, strong shockwaves compress and distort composite materials near the HVI spot [19, 20]. The nonlinear effect of shockwave beyond the Hugoniot elastic limit (HEL) of GF/EP requires the deviatoric strains (ε^d) and the volumetric strain (ε^{vol}) to be demarcated in the form [21]:

$$\begin{bmatrix} \Delta\sigma_{11} \\ \Delta\sigma_{22} \\ \Delta\sigma_{33} \\ \Delta\tau_{23} \\ \Delta\tau_{31} \\ \Delta\tau_{12} \end{bmatrix} = \begin{bmatrix} C_{11} & C_{12} & C_{13} & 0 & 0 & 0 \\ C_{21} & C_{22} & C_{23} & 0 & 0 & 0 \\ C_{31} & C_{32} & C_{33} & 0 & 0 & 0 \\ 0 & 0 & 0 & C_{44} & 0 & 0 \\ 0 & 0 & 0 & 0 & C_{55} & 0 \\ 0 & 0 & 0 & 0 & 0 & C_{66} \end{bmatrix} \begin{bmatrix} \Delta\varepsilon_{11}^d + \frac{1}{3}\Delta\varepsilon^{vol} \\ \Delta\varepsilon_{22}^d + \frac{1}{3}\Delta\varepsilon^{vol} \\ \Delta\varepsilon_{33}^d + \frac{1}{3}\Delta\varepsilon^{vol} \\ \Delta\gamma_{23} \\ \Delta\gamma_{31} \\ \Delta\gamma_{12} \end{bmatrix}$$

(1)

where x, y = 1, 2, 3 are the material directions; $\Delta\sigma_{xy}$ and $\Delta\varepsilon_{xy}$ are the stress and the strain increments, respectively; C_{xy} is the stiffness coefficient. The global Z-axis followed the 11-direction, i.e., the through-thickness material direction. The X-axis and the Y-axis were oriented, respectively, in the 22-direction and the 33-direction, both in-plane (see Fig. 1), due to the prerequisites of the Autodyn hydrocode [22].

Equation of State

A polynomial formulation of Mie-Grüneisen equation of state (EOS) defined the volumetric thermodynamic response of GF/EP to the shockwave pressure [23, 24]:

$$P = K'\mu + A_2\mu^2 + A_3\mu^3 + (B_0 + B_1\mu)\rho_0 e$$
$$\text{when } (\mu > 0, \text{ compression})$$

(2)

$$P = T_1\mu + T_2\mu^2 + B_0\rho_0 e \quad \text{when } (\mu < 0, \text{ expansion})$$ (3)

where volumetric strain, $\mu = (\rho_0/\rho) - 1$.

"0" in subscript is the state prior to the nucleation of shockwave; ρ_0 is the material density prior to the shockwave compression; K is the effective bulk modulus; P, ρ, and e are, respectively, the hydrostatic pressure, the density, and the specific internal energy following the shockwave compression; A_2, A_3, B_0, B_1, T_1, and T_2 are the material constants. The impetus to implement the polynomial EOS came from the modeling flexibility it offered [25].

Damage Nucleation in GF/EP

The numerical framework incorporated an extended Hill's 3D failure criteria available in the Autodyn hydrocode. Because, the failure criteria took into consideration the orthotropic nature of the failure modes and the influence of progressive material degradation on the load carrying capability of GF/EP laminates. The criteria coupled the failure modes employing three failure surfaces [26]:

(i) For the tensile fiber failure

$$e_{22,f}^2 = \left(\frac{\sigma_{22}}{\sigma_{22,f}}\right)^2 + \left(\frac{\sigma_{12}}{\sigma_{12,f}}\right)^2 + \left(\frac{\sigma_{23}}{\sigma_{23,f}}\right)^2 \geq 1,$$
$$\text{in the 22-direction } (\sigma_{22} \geq 0)$$

(4)

where $e_{22,f}^2$ is the failure surface of the corresponding failure mode; f denotes the initial failure strength. The parabolic stress-based failure initiation criterion, when reached the value of 1 or greater than 1 at an element integration point, triggered the failure mode there. The computation cycles checked and updated the failure status of element integration points successively.

Damage Growth in GF/EP

Once a discrete element began to fail, a linear reduction of the corresponding failure stresses updated the stress state of the damaged element. When introduced the linear strain-softening in the Hill's 3D failure criteria, Eq. (4) transformed to [1]:

$$e_{22,f}^2 = \left(\frac{\sigma_{22}}{\sigma_{22,f}(1-D_{22})}\right)^2 + \left(\frac{\sigma_{12}}{\sigma_{12,f}(1-D_{12})}\right)^2 + \left(\frac{\sigma_{23}}{\sigma_{23,f}(1-D_{23})}\right)^2 \geq 1$$

(5)

where D_{xy} is the damage coefficient. $D_{xy} = 0$ indicated the failure initiation and was set to unity as soon as the material

strength was entirely exhausted. The material model of Al is briefly outlined in Appendix.

Debonding Criteria

Unless poorly manufactured, the composite lamina interfaces of FMLs barely delaminate when subjected to a high impulsive load [27]. The proposed GLARE model, to be pertinent, accommodated only Al-GF/EP but no GF/EP-GF/EP interfaces. Surface-to-surface contacts generated detachable bonds between the mating Al layers and the GF/EP composite laminates. A quadratic nominal stress-based criterion [28]:

$$\left\{ \frac{\sigma_n}{\sigma_N} \right\}^a + \left\{ \frac{\sigma_s}{\sigma_S} \right\}^b \geq 1 \quad a, b = 2 \quad (6)$$

when met initiated the debonding of Al-GF/EP interfaces. In Eq. (6), σ_n and σ_s are the stresses in the normal direction and the shear direction of an interface; σ_N and σ_S are the limiting nominal stresses for the normal-only and the shear-only mode of interface debonding. The accessible experimental facilities did not allow measuring the Al-GF/EP interface strength at a high strain-rate. Therefore, $\sigma_N = 8.2$ MPa and $\sigma_S = 46.6$ MPa, respectively, from quasi-static peel and three-point bending experiments were implemented as the approximate Al-GF/EP interface strength. The numerical code invoked a surface interaction between the Al layers and the GF/EP composite laminates subsequent to the interface debonding.

Numerical Implementation

The reference frame of numerical analysis was ALE, since it could discriminate the material interfaces during the long duration penetration phase [29]. Moreover, the ALE method allowed arbitrary adaptation of the element shape in the distorted impact zones. When failure criteria were satisfied at all element integration points, ceased elements eroded into particles. The explicit integration scheme preserved the inertia or the nodal mass at all activated nodal degrees of freedom following the element erosion.

The Autodyn-3D hydrocode adjusted the time-step size based on the shockwave velocity and the element size. A time step size between 0.0002 and 0.002 μs satisfied the convergence criterion of Courant–Friedrichs–Lewy (CFL ≤ 1). Each analysis took over 720 clock hours in a 20 CPU + 100 GB RAM cluster. The computation was terminated as soon as the shockwave and the release waves disappeared from the computational domain, and the kinetic energy of the system approached toward an asymtote.

Material Data

Material Properties of GF/EP

An experimental campaign was pursued in-house to derive the GF/EP laminate properties. The main objective of this paper is to lend detailed insights into the numerical model and its validation. The test methods of material characterization will be elaborated in a companion study, therefore.

Results

Shockwave and Penetration

The numerical analysis treated the HVI damage of GLARE in two distinct phases: (i) short duration phase-I dilatational compression, and (ii) long duration phase-II penetration. Taking the HVI event at $V_I = 7.11$ km/s for instance, Figs. 2 and 3 delineate the two phases.
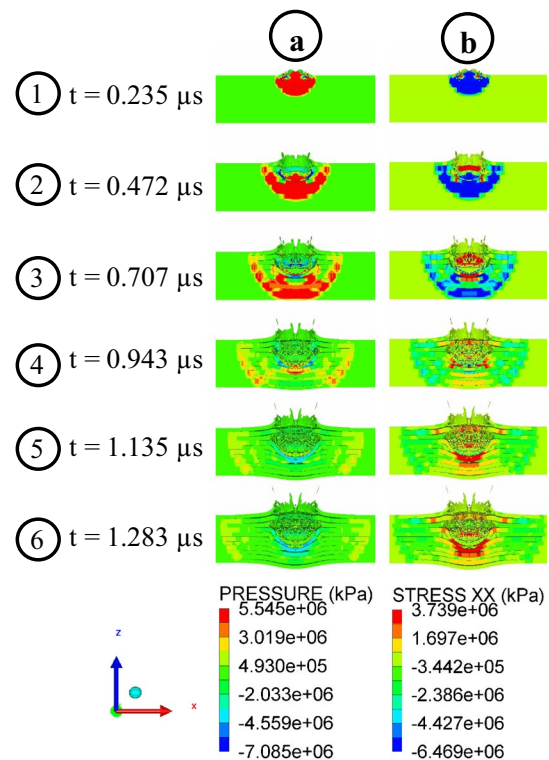
Fig. 2 Short duration phase-I dilatational compression for $V_I = 7.11$ km/s; the pressure scale reads: red color: compression, blue color: expansion; the color annotation is opposite for the stress scale; the upper threshold of color map is reduced to enhance the color contrast
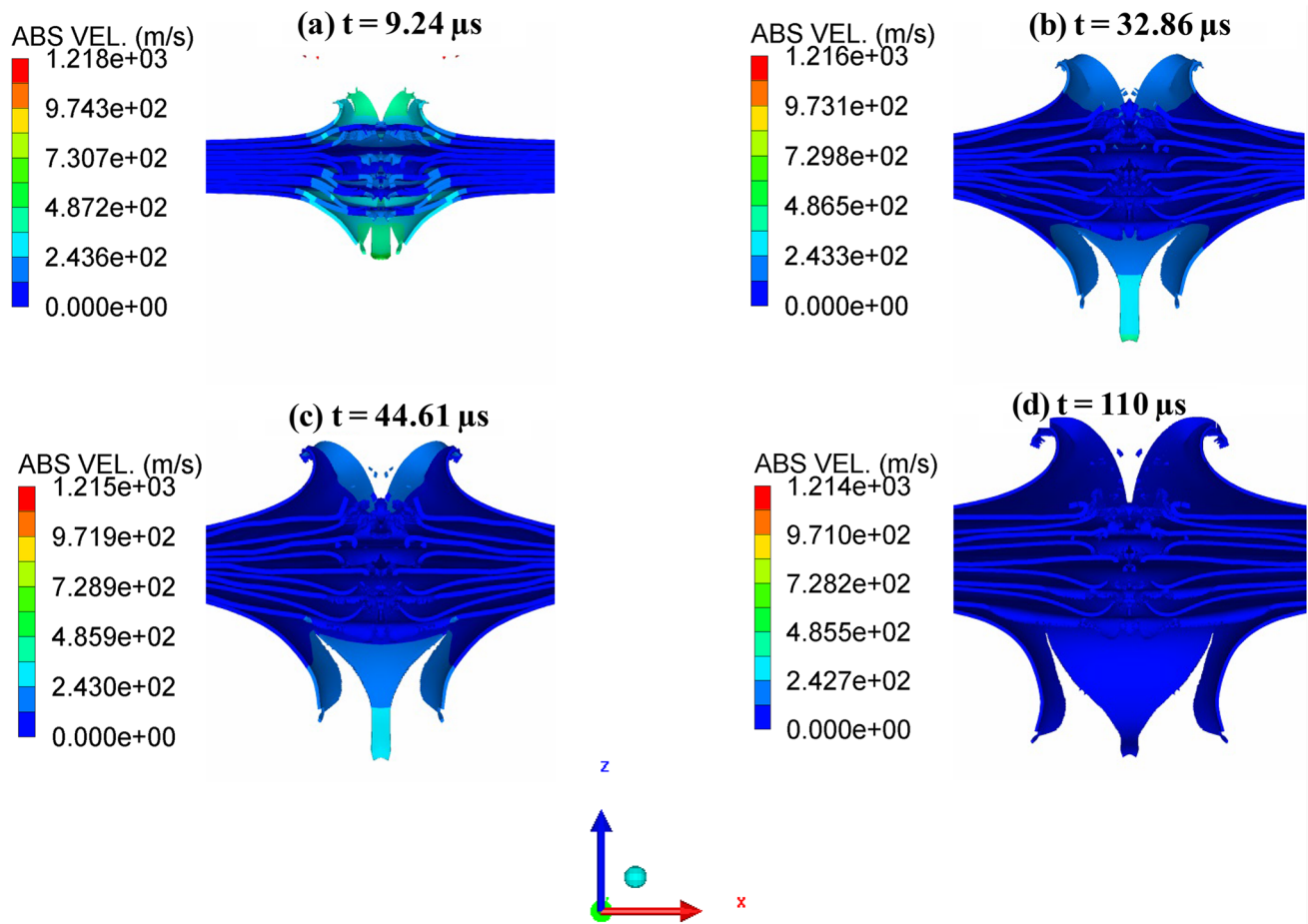
Fig. 3 Progressive HVI damage of GLARE at the long duration penetration phase-II for a normal impact of an Al sphere at V_I = 7.11 km/s

Short Duration Phase-I Dilatational Compression

At $t = 0.235$ μs, the elastic–plastic precursor of compressive stress, at the lip of the shockwave, reached 2.19 mm through the GLARE thickness and compressed the partaking materials (Fig. 2). The in-plane ($\sigma_{xx} = \sigma_{22}, \sigma_{yy} = \sigma_{33}$) and the through-thickness ($\sigma_{zz} = \sigma_{11}$) normal stresses locally traversed the compression regime between -2.58 and -54.9 GPa at the impact site.

At $t = 0.707$ μs, the projectile penetrated 2.35 mm of the GLARE thickness, and the shockwave arrived the rear face of the GLARE laminate. Debonding of the first three predefined interfaces adjacent to the impact site initiated due to the transverse shear and the in-plane compression of pierced material layers.

At $t = 0.943$ μs, the compressive stress wave reflected back as a tensile stress wave from the rear face of the GLARE laminate. The compressive stress wave circumscribed the reverberated tensile stress wave and propagated laterally at an average velocity of 7.34 km/s, which was measured at $t = 1.135$ μs and 7.52 mm in-plane lateral distance from the HVI spot. The release wave did overtake the compressive stress wave and attenuated the shockwave pressure. At $t = 1.135$ μs, the onset of debonding of the farthest interlaminar interface was visibly distinct. Meanwhile, debonding of the frontal three interfaces continued to grow, and dynamic bulging of the GLARE rear face initiated. Next to the shockwave compression phase-I, the long duration penetration phase-II commenced and reinforced further interface debonding and progressive material damage of the GLARE laminate.

Long Duration Phase-II Penetration

Following that, at $t = 9.24$ μs, decompression of the GLARE laminate started, petalled area of the front face enlarged, and the pierced hole of the rear face widened (Fig. 3). Thinning instability of the Al-1 layer (rear face) augmented the fragmentation process. At this instant, the debonded GF/EP-5-laminate, next to the front face (Al-6 layer), flapped backward due to the release from volumetric compression, which resulted into a momentum imbalance and consequently, torn

off the petal tips. In the later time steps, fractures of the front face and the rear face propagated laterally, discernible at t = 32.86 μs. The debonding was less confined to the HVI spot and emanated toward the edge of GLARE. Effective plastic deformation pursued the same trend. The volumetric strain of materials, however, was minute toward the periphery of the target. The inner Al layers buckled under compression and as a result, led to a near symmetric out-of-plane deformation of GLARE related to the GLARE mid-thickness plane. The plate accumulated most of the plastic damage at t = 44.61 μs and reached the permanent deformed state at t = 130 μs, following the recovery of the large transient deformations.

Tensile Failure

Given that the in-plane tensile stress was beyond the limiting threshold, the GF/EP composite laminates collapsed in the fiber failure mode, while the in-plane compressive stress buckled the Al layers. Figure 4 represents the spatial time history of σ_{xx} of GLARE material layers. The σ_{xx} stress profiles stand for the elements at the target center, where the material strain-rate peaked the highest.

Attributed to the enormous volumetric compression ratio of 0.49 at the projectile/target contact spot, the Al-6 elements failed immediately upon impact. The bulk failure of Al-6 layer (front face) let the projectile downstream to the GF/EP-5 composite laminate. The GF/EP-5 composite laminate, next at t = 0.442 μs, experienced a tensile σ_{xx} stress of + 7.38 GPa due to membrane stretching, which was greater than the corresponding tensile strength (σ_{xxf} = + 0.59 GPa) of the cross-ply composite laminate (look at Table 1). The beyond limiting tensile stress allowed orthotropic softening of composites and degraded the GF/EP-5 elements in the fiber failure mode at t = 0.597 μs (see Fig. 4). The distal GF/EP composite laminates succumbed to similar progressive softening and were pierced when met the failure stress. At

t = 1.01 μs, the rear half of the GLARE laminate was under in-plane tension and did not turn back to the compression regime. Because, local bending and lateral release waves, emanated from the periphery of GLARE laminate, attenuated the compressive stress.

The chronological failure of material layers resulted in the perforation of GLARE laminate at t = 3.39 μs. The successive failure of material layers elongated the zero σ_{xx} stress line from the GLARE front (H/H_G = 0) face to rear face (H/H_G = 1) in the progressive time steps.

Strain-Rate

The selected GLARE grade belonged to the thick laminates attributed to its thickness to projectile diameter ratio of 2.5. To dissipate the impact energy, the GLARE laminate preferred local- compression and bending instead of global deformation, therefore. Besides, the bulk modulus of GF/EP composite was only 1/5.3 times the shockwave-induced pressure, which helped a significant through-thickness compression of the GLARE laminate at an exorbitant strain-rate (see Fig. 5).

Among the material layers, the highest compressive strain-rate $\dot{\varepsilon}_{zzc}$ = 87.61 μs^{-1} of the frontal Al-6 layer cracked the Al elements upon impact and was circa 8.4 times the corresponding $\dot{\varepsilon}_{zzc}$ experienced by the mating GF/EP-5 composite laminate. Distal Al layers suffered a lower $\dot{\varepsilon}_{zzc}$, estimated a maximum 16.85 μs^{-1} in the Al-4 layer, which was, yet, 13 μs^{-1} higher than that of the adjacent GF/EP-3 composite laminate. Ascribed to the astronomical strain-rate, the viscous pressure of Al layers was enormous than that sustained by the GF/EP composite laminates. The Al layers, consequently, collapsed earlier than the GF/EP composite laminates that justified the failure chronology of mating material layers explicated in Sect. 6.2.

Fig. 4 Spatial time history of normal stress (σ_{xx}) through the GLARE thickness for V_I = 7.11 km/s; zero and one of the normalized GLARE thickness (H/H_G) indicate the front face and the rear face, respectively
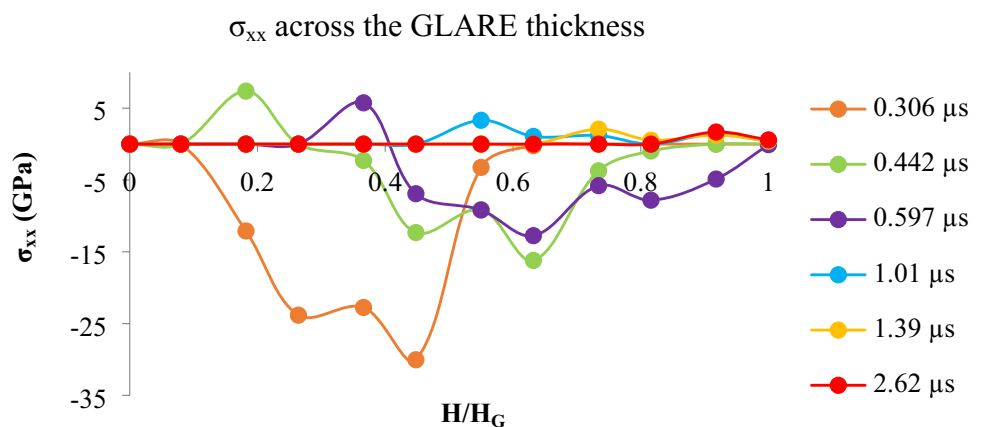
(a) Strain-rate of Al layers

(b) Strain-rate of GF/EP composites
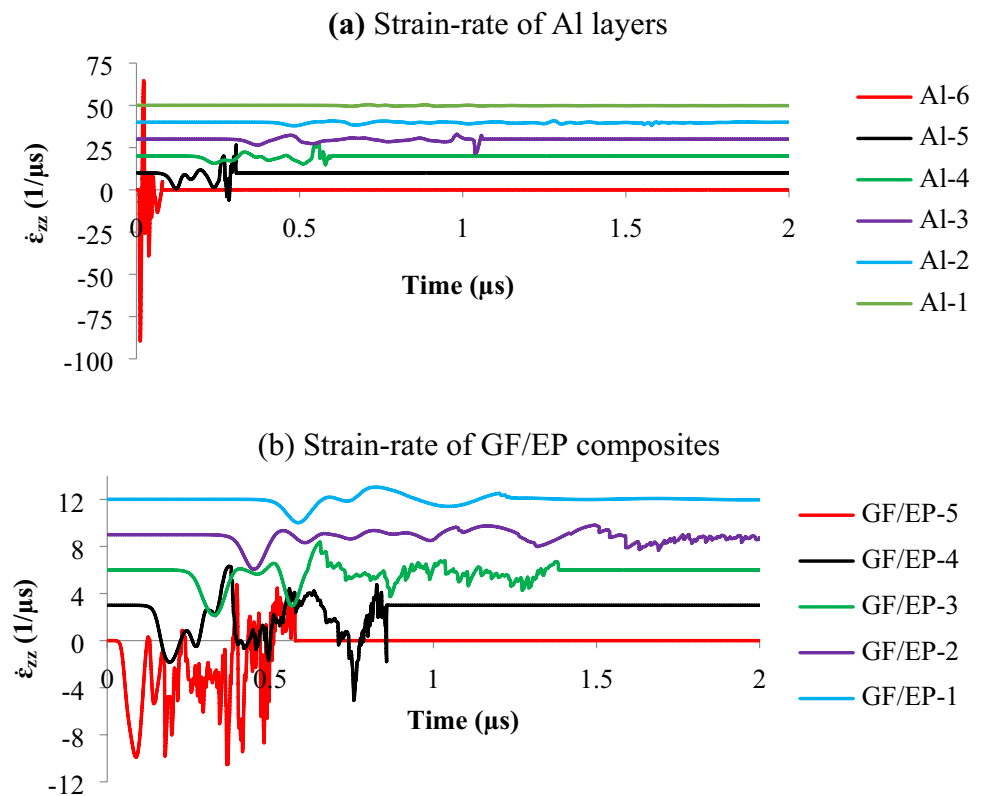
Debris Clouds

The energy, not dissipated in the shockwave, remained as disruptive kinetic energy of GLARE and exerted forces causing fragmentation and dispersion of the debris cloud. The debris plume emanated when Al elements eroded upon reaching the failure strain in the three normal and the three shear directions. The GF/EP elements, if failed at eight integration points, eroded as well. With the aid of the erosion scheme, HVI of a 2 mm Al-sphere on a GLARE 5–6/5–0.4 laminate at $V_I = 7.11$ km/s evacuated debris clouds uprange and downrange (Fig. 6). The uprange debris veil ejected in a tapered axisymmetric conical shape fringed by the eroded particles of Al layers. The GF/EP-debris and the projectile remnants densely populated the veil core. The debris density evolved to be sparser with time and formed a larger spreading angle, attributed to the continuous lateral dispersion of disrupted debris mass (compare Fig. 6b with 6d).

At a later instance, a debris cloud ejected downrange courtesy to the onset of tensile fracture of the rear Al-1 layer (Fig. 6b). Details of the GF/EP-debris jetting laterally from the perforated hole were apparent. While the Al-debris packed the leading edge of downrange ejecta in the axial direction, the GF/EP-debris trailed back the Al-remnants and dispersed in the diametral direction due to the surface drag on the debris particles (Fig. 6d). At $t = 21.05$ μs, the leading edge (point 1 of Fig. 6a) of the behind-target debris

cloud attained an axial velocity of 1.81 km/s at 3.45 cm downstream distance from the rear face. At $t = 67.86$ μs, the debris particle at point 2 (see Fig. 6c) travelled a downstream distance of 6.14 cm at a velocity 977.58 m/s, which was in correspondence with the experiment, wherein a debris velocity of 939.85 m/s was determined. At $t = 104.7$ μs, the cloud leading edge arrived at 16.14 cm downstream distance, where the axial velocity declined to 1.15 km/s. The debris mass at the cloud leading edge was negligible, however. The appreciable axial velocity, therefore, will cease to impart any critical damage to the spacecraft bulkhead. By contrast, the debris particle at point 3 (see Fig. 6c) dispersed laterally at a dissimilar velocity, predicted 224 m/s at $t = 67.86$ μs; next, inclined to 252.05 m/s at $t = 104.7$ μs. The lateral dispersion of the debris emerged substantial, the axial dispersion of the debris cloud was limited albeit.

Perforated and Non-perforated Deformation

Test Instruments

To validate the numerical model, a two-stage light-gas gun was employed to conduct the HVI experiments on GLARE specimens at room temperature and 50% relative humidity. Helium was used as the propellant. Figure 7a includes a pictorial image of the test set-up and Fig. 8 outlines the basic lay-out of the gas gun. At the end of the target chamber, 4
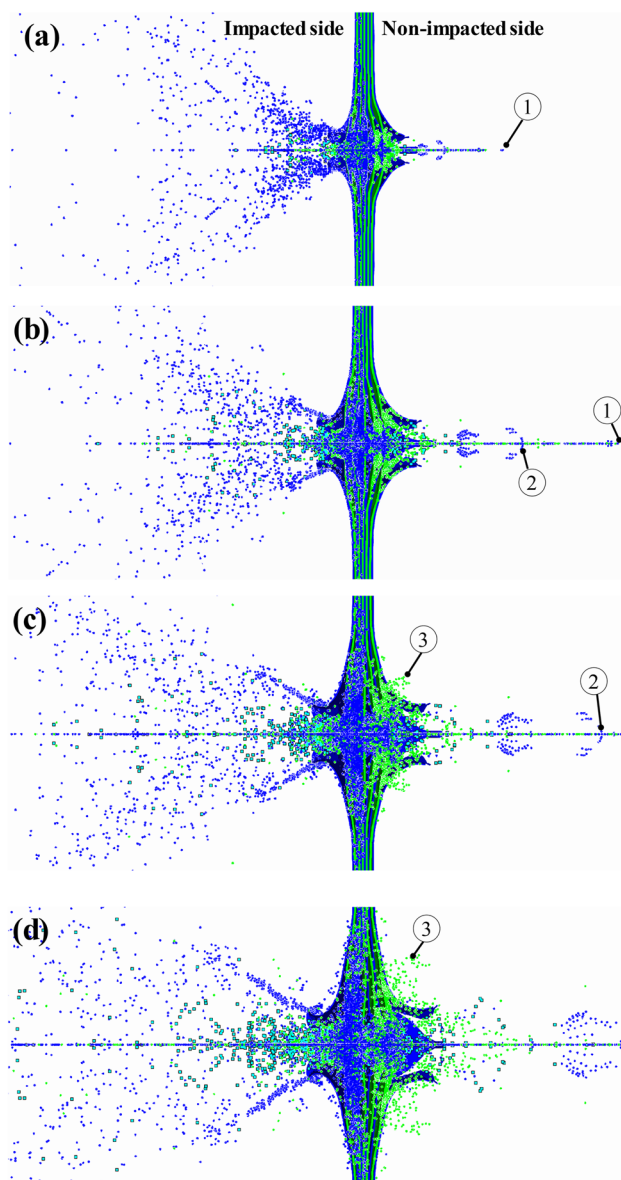
Fig. 6 The temporal evolution of uprange and downrange debris clouds for the hypervelocity impact on GLARE at $V_I = 7.11$ km/s at **a** $t = 21.05$ μs, **b** 44.61 μs, **c** 67.86 μs, **d** 104.7 μs; 1 and 2 stand for the particles, which were tracked to measure the axial velocity; 3 indicates the particle associated with the radial velocity measurement

bars on a hatch kept the target plate fixed against the projectile. A witness plate, placed 60 mm downstream of the GLARE plate, collected the debris cloud that comprised fragmented projectile and GLARE materials. Two wide beam lasers, positioned perpendicular to the projectile trajectory, measured the impact velocity within ± 0.01 km/s. A vibration sensor, attached to the GLARE plate, verified the impact velocity determined by the laser beams. An identical sensor on the witness plate helped measure the impingement velocity of the downrange debris cloud. To measure the velocity of downrange debris, first, the time required

for the leading edge of the debris cloud to impact the witness plate and next, for the impingement signal to reach the vibration sensor on the witness plate were measured. High-speed videos of the HVI events could not be captured, since a high-speed camera of a million frame rate was not available during the test campaign. The explosive nature of HVI destroyed the surface-adhered thermocouples a couple of times. To avoid further damage of the test assets, the test plan did not include measuring the temperature gradient of GLARE specimens upon impact.
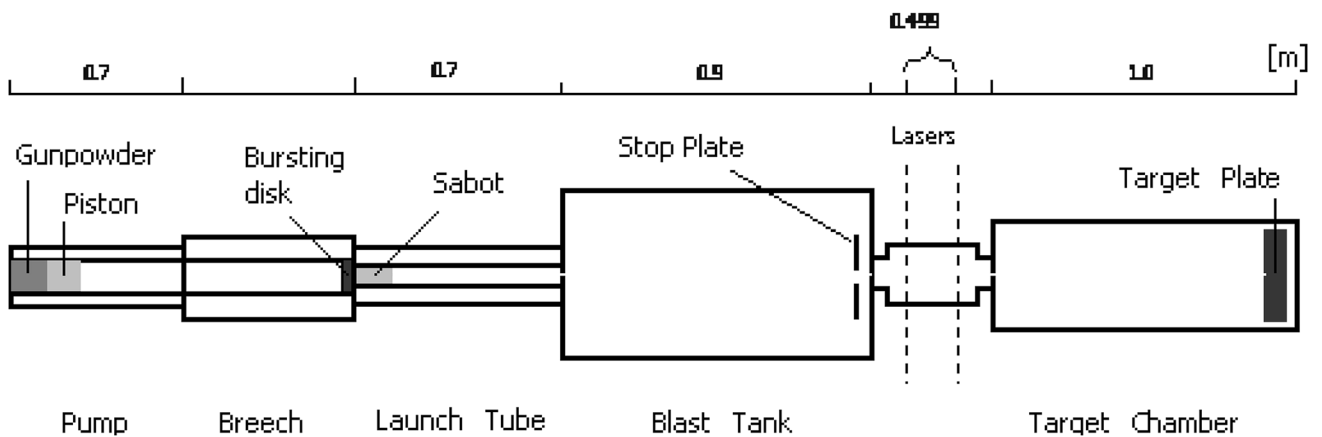
Quantitative Assessment: Petals

Figure 9 compares the numerical predictions against the experimental outcomes. The quarter GLARE model was reflected about the two symmetry planes for a better pictorial analysis. As found, the distinctive features of GLARE damage were the fracture and the outward petals of the front face around the central perforated hole. When the impact velocity increased from 4.78 to 7.11 km/s, the front face petalled area reshaped from a near circular to an elliptical contour (compare Fig. 9a, c). At $V_I = 4.78$ km/s, the non-perforated rear face sustained a crack at the tip of the circular cusp due to plastic yielding (Fig. 9b). By comparison, at $V_I = 7.11$ km/s, the rear face ruptured and generated a near rectangular petalled area (Fig. 9d). The shape of the petalled areas was consistent with that of the test specimens. At both impact velocities, perforated holes of the GF/EP composite laminates had smaller openings than the holes pierced in the Al layers, in agreement with the experiments.

At $V_I = 4.78$ km/s, the ten front face petals of the test specimens were way more than the four front face petals predicted by the analysis (Fig. 9a; Table 3). If compared, HVI at $V_I = 7.11$ km/s generated eight front face petals both in the experiment and the simulation (Fig. 9c; Table 3); on the flip side, the predicted rear face petals were four compared to seven rear face petals of the test specimen (Fig. 9d; Table 3). HVI at $V_I = 9$ and 11 km/s added no extra front face petals compared to that for the event at $V_I = 7.11$ km/s, but redistributed the eight front face petals around a circular petalled area (Fig. 9e, g; Table 3). It is anticipated that the front face became fracture-saturated beyond the ballistic limit and dissipated the excess energy through thinning, buckling and transient vibration. Conversely, the rear face petals were identical in number (counted four) at $V_I = 7.11$ and 9 km/s (Fig. 9d vs 9f, Table 3). On the other hand, at $V_I = 11$ km/s, the rear face petals multiplied to eight and were four more than that at $V_I = 7.11$ km/s (Fig. 9h vs 9d, Table 3). Unlike the near rectangular rear face petalled area at $V_I = 7.11$ km/s, the HVI at $V_I = 11$ km/s inscribed an elliptical petalled area at the rear face.
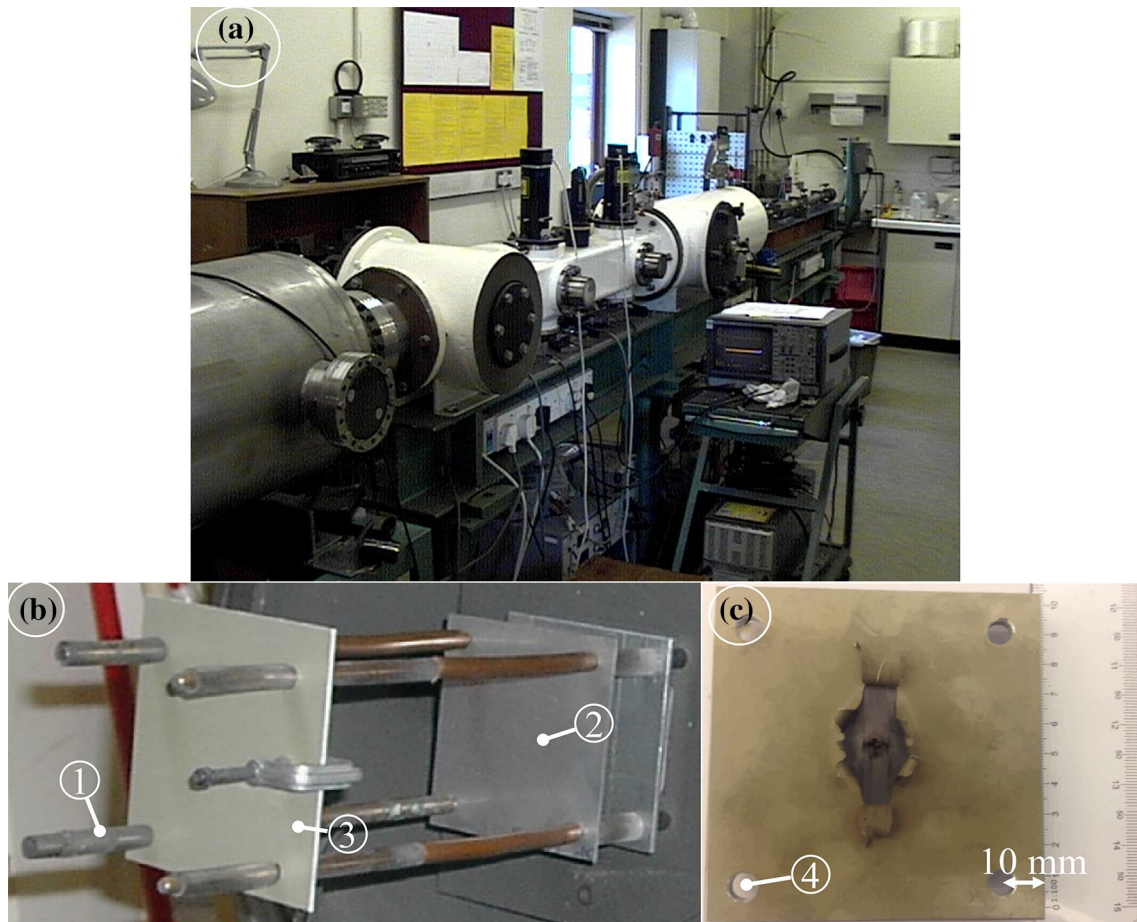
Fig. 7 **a** The two-stage light-gas gun; **b** the mounting hatch; **c** a GLARE specimen subjected to HVI; 1 and 2 stand for the mounting bar and the witness plate; 3 identifies the GLARE plate on the mounting bars; 4 indicates the location of bored holes


Fig. 8 Schematic side-view of the two-stage light-gas gun

Qualitative Assessment: Permanent Deformation and Debonding

Figure 10 shows that the predicted out-of-plane deformation of GLARE was beyond the experimental one at $V_I = 4.78$

and 7.11 km/s. The model over-predicted debonding compared to that of the test specimens. Updating the strength and the mode-mixity of model interfaces, based on the hyper-strain-rate 10^4–10^6 s^{-1} [24, 30], will alleviate the deformation discrepancies.
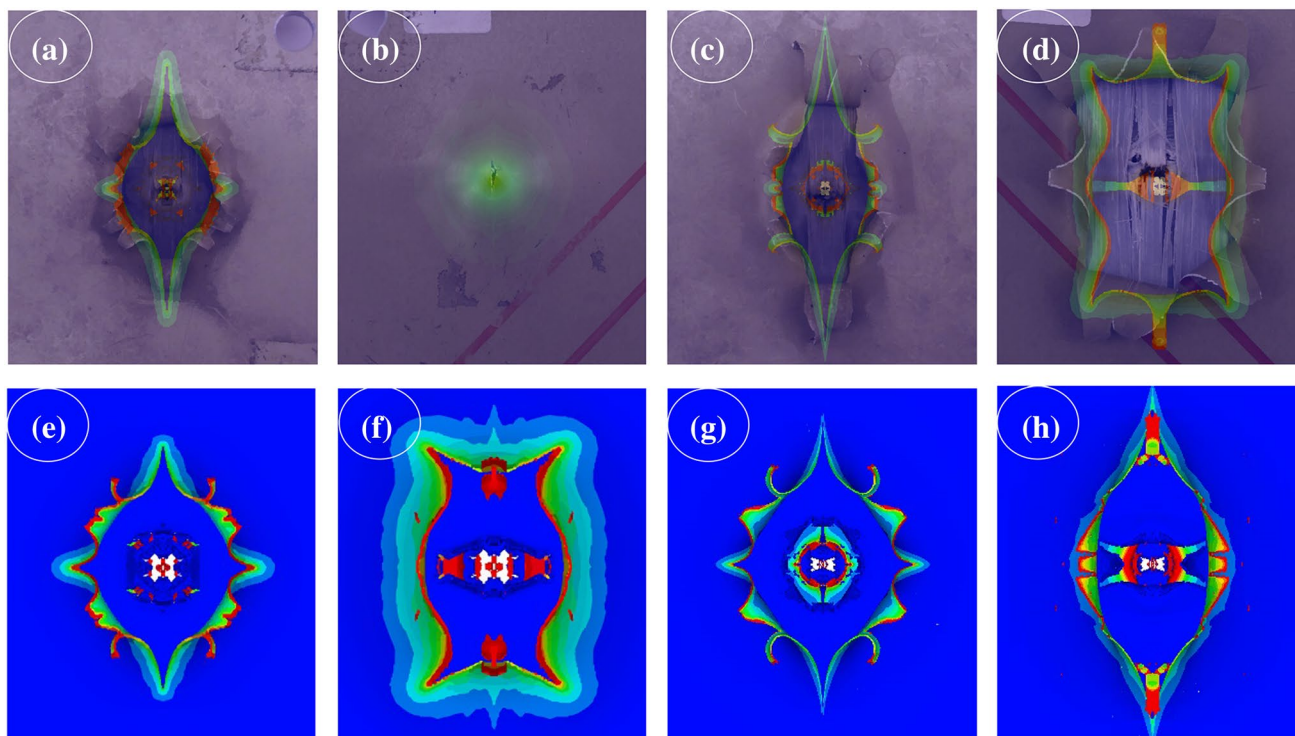
Fig. 9 Comparison of predicted petals against experimental ones; **a**, **b** correspond, respectively, to the front face and the rear face damage for $V_I=4.78$ km/s; **c**, **d** stand, respectively, for the front face and the rear face petals for $V_I=7.11$ km/s; **e**, **f** show, respectively, the front face and the rear face petals for $V_I=9$ km/s; **g**, **h** demonstrate, respectively, the front face and the rear face petals for $V_I=11$ km/s; computation time 130 μs

Table 3 Petals in experiments and simulations

GLARE panel	V_I (km/s)	Front face petals		Rear face petals	
		Measurement	Prediction	Measurement	Prediction
GLARE 5-6/5-0.4	4.78	10	4	NP	NP
	7.11	8	8	7	4
	9		8		4
	11		8		8

NP no perforation; the counted petals correspond to the pictorial images in Fig. 9

Quantitative Assessment

Perforated Holes For the quantitative assessment, diameter of the perforated holes in the front and the rear face were compared (Table 4). The digital images, shown in Fig. 9, were post-processed to take the scale measurements between the two closest points of the perforated holes in the outer Al-skins. Quantitative assessments revealed that the numerical model predicted a 11 mm wide damage against the 17.67 mm wide damage determined in the experiments, thus, underestimated the front face failure at $V_I=4.78$ km/s.
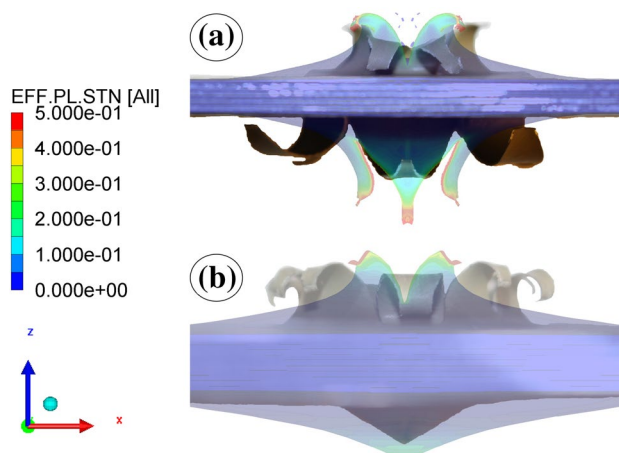
Fig. 10 Predicted out-of-plane deformation contours against the experimental outcomes; **a**, **b** stand for $V_I=7.11$ and 4.78 km/s, respectively; the predicted contour at 4.78 km/s is magnified to facilitate the comparison with the experimental one

However, the predicted front face failure (16 mm) was in close agreement with that (14.40 mm) of the test specimen at $V_I=7.11$ km/s. This velocity inflicted a non-conservative rear face failure (predicted 18.5 mm) against that

Table 4 Measured and predicted failures in comparison

GLARE panel	V_I (km/s)	Front face failure, mm		Difference, % ((M–P)/M)*100	Rear face failure, mm		Difference % ((M–P)/M)*100
		Measured	Predicted		Measured	Predicted	
GLARE 5-6/5-0.4	4.78	17.67	11	37.74	NP	NP	
	7.11	14.40	16	− 11.11	25.21	18.5	26.61
	9		24.3			20.2	
	11		37.7			22.6	

NP no perforation, *M* measured, *P* predicted; the measured damage width corresponds to the pictorial images in Fig. 9

Table 5 Dissipated impact energy in tests and simulations

GLARE panel	V_I (km/s)	% impact energy dissipated		Difference, % ((M–P)/M)*100
		Measured	Predicted	
GLARE 5-6/5-0.4	4.78	51.5	58	− 12.5
	7.11	62.2	69.9	− 12.3
	9		87.6	
	11		91.4	

M measured, *P* predicted

(25.21 mm) of the test specimen. The front face and the rear face succumbed to more damage with the impact velocity. As found at $V_I = 9$ km/s, the front face failure widened to 24.3 mm. The 11 km/s impact further enlarged the front face failure to 37.7 mm. The front face failure exponentially inclined with the impact velocity. By contrast, the relation of predicted rear face failure to the impact velocity was near linear, showing a mere 4 mm wider rear face failure when V_I inclined from 7.11 to 11 km/s.

Dissipated Energy In experiments, the only viable way to approximate the energy dissipated in GLARE damage is: subtract the debris cloud energy from the total impact energy. The energy of the debris cloud is a function of the debris mass and the debris velocity. Since the Al projectile entirely vaporized upon impact, the mass difference of the target plate prior and posterior to the HVI test resulted in the erupted debris mass. The vibration sensor on the witness plate helped measure the velocity of the debris cloud, by considering the time needed for the leading edge of the debris cloud to impinge the witness plate, and for the impingement signal to reach the vibration sensor on the witness plate. Whilst the estimated debris mass and debris velocity were taken into consideration, the experiments demonstrated that circa 51.5 and 62.2% of the projectile impact energy dissipated in the GLARE damage for $V_I = 4.78$ and 7.11 km/s, respectively.

Now, look at the numerical analysis: the GLARE damage dissipated circa 58 and 69.9% of the projectile impact energy for $V_I = 4.78$ and 7.11 km/s, respectively. The predicted energy dissipation was equal to the total energy dissipated in the plastic damage of GLARE at the end time step of computation. The energy budget for plastic damage subsumed the energy budget for Al-GF/EP interface debonding, plastic deformation and mass erosion of GLARE constituents. The validation confirmed predicted values within appropriate tolerance limits of the experimental estimations (see Table 5). As the V_I increased to 9 and 11 km/s, the dissipated energy reached, respectively, 87.6 and 91.4% of the projectile impact energy. The energy saturation of the GLARE laminate beyond the shatter regime made the increase of energy dissipation inconspicuous. The extent of irreversible work accomplished by the GLARE laminate implies that the energy flux density to the spacecraft bulkhead will be less, which makes the GLARE laminate a potential candidate for a protection shield against micrometeoroids.

Discussion and Conclusions

Analyzing the HVI, damage modes and perforation of thick GLARE laminates is complex and demands a continuous assessment of the spatio-temporal energy equilibrium of the computational domain. This study envisaged the analysis using an explicit dynamics FE-model of GLARE in the state-of-the-art hydrocode Autodyn. At $V_I = 4.78$ and 7.11 km/s, It was found that the model predicted many of the experimental observations with a high degree of fidelity. Next, the validated model was further implemented to interrogate the physical phenomena of GLARE damage at $V_I = 9$ and 11 km/s.

Of notes, many relevant studies on the impact resistance of GLARE focused on developing numerical models to reconstruct the experimental events only without justifying the physical reasons behind the damage accumulation of GLARE. The evacuation of the debris ejecta out of GLARE had been rarely addressed, the ricochet debris can damage the spacecraft external service components albeit. The packing of debris particles directly stands for the degree

of damage sustained by a GLARE laminate upon HVI. This study, therefore, employed a model that could capture the HVI-induced shockwave, disrupted debris mass of GLARE, while predicted two distinct phases of GLARE damage evolution.

In the short duration dilatation phase, the impact-induced shockwave generated a lethal compression ratio of 0.49 at the HVI spot for $V_I = 7.11$ km/s, resulting in the bulk failure of material at the impact site. Toward the rear face, the shockwave pressure dropped ascribed to the wave breaking at the interlaminar interfaces (see Fig. 2). The damage of material was minute toward the GLARE periphery. Because, the compression-decompression of material dissipated the shockwave energy through deformation-induced plasticity, commensurate with the plastic hardening of Al and stiffness degradation (orthotropic softening) of GF/EP. The pressure of shockwave declined in the radial direction and the GLARE damage circumscribed the impact zone, as a result. The stress waves preferred the fiber direction to propagate. Because the orderly crystalline morphology of glass fibers allowed a barrier-free wave trajectory. The outcomes imply that a multiplex fiber orientation helps predetermine the path of a shockwave and confine the shockwave energy and the material damage into a limited area.

The long duration penetration phase promoted the debonding of GLARE and split the GLARE laminate stack into sub-laminates. Since the sub-laminates possessed a buckling stiffness lower than the corresponding stiffness of the pristine GLARE laminate, the AL-GF/EP interfaces favored the normal mode of failure. The normal strength of GLARE interfaces needs to be improved to apportion a higher energy between debonding and delamination and reinforce the bending stiffness and the related impact resistance of a GLARE laminate.

During penetration, the GLARE mass started to disrupt as soon as the release waves decompressed the GLARE laminate, which was evident by the outward volumetric expansion of the GLARE laminate (see Fig. 10). The perpetual release waves fragmented the projectile with the help of viscous pressure and helped the debonded GF/EP composite laminates to radially disperse the projectile momentum. The membrane stretching of GF/EP attenuated the axial momentum of the projectile, while conserved 85.62% of the total elastic energy of GLARE for $V_I = 7.11$ km/s. The frontal Al-skins sustained a large scale damage, discernible by the dense packing of Al particles of the uprange debris cloud. Because, first the frontal material layers encountered the meteoric kinetic energy and the momentum of the projectile. The erosion-committed fracture and the plastic deformation of Al layers contributed, respectively, a large 64.61 and 32.08% to the plastic damage energy of GLARE

for $V_I = 7.11$ km/s. It is noticeable that the eroded GF/EP particles were circa 100 folds lower in number than that of the Al particles of the debris cloud, which implied a lower scale damage of GF/EP composite laminates, as found in the experiments.

The delineated damage mechanism suggests that a higher number of material layers will reinforce the pressure drop of shockwave through the GLARE thickness, attributed to the more interlaminar interfaces that help disperse the shockfront. Given the shockwave pressure disappears before the reach of the rear face, the wave reflection at the free surface and the spallation of GLARE can be prevented. The mismatch of fiber orientation of mating GF/EP plies confines the shockwave expansion by dispersing the shock-front. Quasi-isotropic (0°/+45°/−45°/90°) GF/EP composite laminates, correspondingly, constrain the shockwave-committed damage area. Thicker Al-skins multiply the viscous pressure at the HVI spot and help fragmenting the projectile. In companion, thinner Al-skins allocate an appreciable impact energy to the membrane stretching of GLARE. Looking at the HVI damage it can be concluded that a thick GLARE configuration, comprises a higher volume fraction (0.7) of quasi-isotropic GF/EP composite laminates than that (0.3) of Al sheets, will be suitable for spacecraft structures. Keeping the volume fraction of GF/EP, numerous composite laminates, alternately stacked between Al sheets, offer a recurring change of wave impedance through the GLARE thickness. The gradient of wave impedance helps abate the shockwave amplitude and reduce the material damage away from the impact site. For a HVI-resistant GLARE configuration, at least two GF/EP composite laminates are recommended. The outer skins of GLARE should be thick Al sheets (0.4 mm or thicker) to crush a micrometeoroid, and the inner Al-skins need to be thinner (max 0.2 mm thick) to reinforce global bending and energy dissipation in elastic deformation.

Though the model predicted many damage modes of GLARE in correspondence to the experiments, it over-predicted interface debonding. That means, the pre-defined interfaces were not strong enough compared to that of the manufactured specimens. An increase of the interface strength will reinforce the bending stiffness of the GLARE model and reduce the out-of-plane deformation. The outcomes suggest to determine the GLARE interface strength at a strain-rate akin to the exorbitant strain-rate of material in a HVI event. However, pursuing such a meteoric strain-rate in double cantilever beam and three point bending test instruments is challenging. Not the least, approximating the sublimation and the outward expansion of epoxy demands measuring the multiphase fraction of epoxy related to the

shockwave-committed material compression, and accommodating the multiphase equations of state in the model to capture the phase transition. Data on the sublimation of epoxy under shockwave-induced pressure and temperature are not readily available in the literature, yet. The disparity between the numerical predictions and the measurements will be reduced, if the model merges the physics of thermodynamics with the solid mechanics and comprises reliable data on material phase change. Any effort to model improvement has to be pursued with a degree of prudence to make the computation less onerous.

Compliance with ethical standards

Conflict of interest The author declares no competing interests.

Appendix

Material Model of Al

The semi-empirical flow stress model of Steinberg–Guinan delineated the strain-rate dependent plasticity of Al layers (see Table 2). The model assumed that at a strain-rate of 10^5 s^{-1}, the yield stress reached the limiting maximum and next, was independent of strain-rate. A shear modulus, proportional to pressure and inversely proportional to temperature, made sure the Bauschinger effect was included in the model. The shear modulus (G) and the yield stress (Y) read:

$$G = G_0 \left\{ 1 + \left(\frac{G_p'}{G_0} \right) \frac{p}{\eta^{1/3}} + \left(\frac{G_T'}{G_0} \right)(T - 300) \right\} \quad (7)$$

$$Y = Y_0 \left\{ 1 + \left(\frac{Y_p'}{Y_0} \right) \frac{p}{\eta^{1/3}} + \left(\frac{G_\tau'}{G_0} \right)(T - 300) \right\} (1 + \beta\varepsilon)^n \quad (8)$$

subject to $\quad Y_0[1 + \beta\varepsilon]^n \leq Y_{max}$

where ε, β, n, T, $\eta = v_0/v$ stand for the effective plastic strain, hardening constant, hardening exponent (see Table 2), temperature, and compression, respectively. The subscripts p and T of primed parameters stand for the derivatives at the reference pressure and temperature ($T = 300$ K, $P = 0$, $\varepsilon = 0$). Subscripts *max* and zero indicate the maximum value and the reference state before the nucleation of a shockwave. The Mie-Grüneisen equation of state correlated the pressure with

the volumetric strain of Al. Material constants, C1 specified the characteristic sound speed in 2024-T3 aluminum alloy and S1 yielded the slope between the shockwave velocity and the particle velocity (see Table 2). Al-elements failed when met the failure strain (see Table 2) in the three normal and the three shear directions.

References

1. Clegg RA, White DM, Hayhurst C, Ridel W, Harwick W, Hiermaier S (2003) Advanced numerical models and material characterisation techniques for composite materials subject to impact and shock wave loading. J Phys IV France 110:311–316. https://doi.org/10.1051/jp4:20030712
2. Greenhalgh ES, Bloodworth VM, Iannucci L, Pope D (2013) Fractographic observations on Dyneema® composites under ballistic impact. Composites A 44:51–62. https://doi.org/10.1016/j.compositesa.2012.08.012
3. Nguyen LH, Ryan S, Cimpoeru SJ, Mouritz AP, Orifici AC (2015) The effect of target thickness on the ballistic performance of ultra high molecular weight polyethylene composite. Int J Impact Eng 75:174–183. https://doi.org/10.1016/j.ijimpeng.2014.07.008
4. Vlot A, Gunnink JW (2001) Fibre metal laminates: an introduction. Springer, Dordrecht
5. McCarthy MA, Xiao JR, Petrinic N, Kamoulakos A, Melito V (2004) Modelling of bird strike on an aircraft wing leading edge made from fibre metal laminates—Part 1: material modelling. Appl Compos Mater 11(5):295–315. https://doi.org/10.1023/B:ACMA.0000037133.64496.13
6. Vlot A (1993) Impact properties of fibre metal laminates. Compos Eng 3(10):911–927. https://doi.org/10.1016/0961-9526(93)90001-Z
7. Cortés P, Cantwell WJ (2007) The impact properties of high-temperature fiber-metal laminates. J Compos Mater 41(5):613–632. https://doi.org/10.1177/0021998306065291
8. Hoo Fatt MS, Lin C, Revilock DM, Hopkins DA (2003) Ballistic impact of GLARE™ fiber–metal laminates. Compos Struct 61(1–2):73–88. https://doi.org/10.1016/S0263-8223(03)00036-9
9. Sitnikova E, Guan ZW, Schleyer GK, Cantwell WJ (2014) Modelling of perforation failure in fibre metal laminates subjected to high impulsive blast loading. Int J Solids Struct 51(18):3135–3146. https://doi.org/10.1016/j.ijsolstr.2014.05.010
10. Langdon GS, Lemanski SL, Nurick GN, Simmons MC, Cantwell WJ, Schleyer GK (2007) Behaviour of fibre–metal laminates subjected to localised blast loading: Part I—experimental observations. Int J Impact Eng 34(7):1202–1222. https://doi.org/10.1016/j.ijimpeng.2006.05.008
11. Guan ZW, Cantwell WJ, Abdullah R (2009) Numerical modeling of the impact response of fiber-metal laminates. Polym Compos 30(5):603–611. https://doi.org/10.1002/pc.20594
12. Karagiozova D, Langdon GS, Nurick GN, Chung Kim Yuen S (2010) Simulation of the response of fibre–metal laminates to localised blast loading. Int J Impact Eng 37(6):766–782. https://doi.org/10.1016/j.ijimpeng.2009.04.001
13. Yaghoubi AS, Liaw B (2014) Influences of thickness and stacking sequence on ballistic impact behaviors of GLARE 5 FML plates: Part I-experimental studies. J Compos Mater 48(16):2011–2021. https://doi.org/10.1177/0021998313494097
14. Fan J, Guan ZW, Cantwell WJ (2011) Numerical modelling of perforation failure in fibre metal laminates subjected to low

velocity impact loading. Compos Struct 93(9):2430–2436. https://doi.org/10.1016/j.compstruct.2011.04.008

15. Garcia M (2015) Space debris and human spacecraft. https://www.nasa.gov/mission_pages/station/news/orbital_debris.html. Accessed 28 May 2019

16. Vlot A (1996) Impact loading on fibre metal laminates. Int J Impact Eng 18(3):291–307. https://doi.org/10.1016/0734-743X(96)89050-6

17. Harding MM, Ruiz C (1997) The mechanical behaviour of composite materials under impact loading. KEM 141–143:403–426. https://doi.org/10.4028/www.scientific.net/KEM.141-143.403

18. Vural M, Ravichandran G (2004) Transverse failure in thick S2-glass/epoxy fiber-reinforced composites. J Compos Mater 38(7):609–623. https://doi.org/10.1177/0021998304042400

19. Gama BA, Gillespie JW (2008) Punch shear based penetration model of ballistic impact of thick-section composites. Compos Struct 86(4):356–369. https://doi.org/10.1016/j.compstruct.2007.11.001

20. Gama BA, Gillespie JW (2011) Finite element modeling of impact, damage evolution and penetration of thick-section composites. Int J Impact Eng 38(4):181–197. https://doi.org/10.1016/j.ijimpeng.2010.11.001

21. Hayhurst CJ, Hiermaier SJ, Clegg RA, Riedel W, Lambert M (1999) Development of material models for Nextel and Kevlar-epoxy for high pressures and strain-rates. Int J Impact Eng 23(1):365–376. https://doi.org/10.1016/S0734-743X(99)00087-1

22. ANSYS/Autodyn 15 (2012) User's Manual. ANSYS Inc, South Pointe

23. Anderson CE, O'Donoghue PE, Skerhut D (1990) A mixture theory approach for the shock response of composite materials. J Compos Mater 24(11):1159–1178. https://doi.org/10.1177/002199839002401104

24. O'Donoghue PE, Anderson CE, Friesenhahn GJ, Parr CH (1992) A constitutive formulation for anisotropic materials

suitable for wave propagation computer programs. J Compos Mater 26(13):1860–1884. https://doi.org/10.1177/002199839202601301

25. Wicklein M, Ryan S, White DM, Clegg RA (2008) Hypervelocity impact on CFRP: testing, material modelling, and numerical simulation. Int J Impact Eng 35(12):1861–1869. https://doi.org/10.1016/j.ijimpeng.2008.07.015

26. Grujicic M, Glomski PS, He T, Arakere G, Bell WC, Cheeseman BA (2009) Material modeling and ballistic-resistance analysis of armor-grade composites reinforced with high-performance fibers. J Mater Eng Perform 18(9):1169–1182. https://doi.org/10.1007/s11665-009-9370-5

27. Langdon G, Nurick G, Lemanski S, Simmons M, Cantwell W, Schleyer G (2007) Failure characterisation of blast-loaded fibre–metal laminate panels based on aluminum and glass–fibre reinforced polypropylene. Compos Sci Technol 67(7–8):1385–1405. https://doi.org/10.1016/j.compscitech.2006.09.010

28. Yaghoubi AS, Liaw B (2014) Influences of thickness and stacking sequence on ballistic impact behaviors of GLARE 5 FML plates: Part II—numerical studies. J Compos Mater 48(19):2363–2374. https://doi.org/10.1177/0021998313498104

29. Anderson CE (1987) An overview of the theory of hydrocodes. Int J Impact Eng 5(1–4):33–59. https://doi.org/10.1016/0734-743X(87)90029-7

30. Anderson CE, Cox PA, Johnson GR, Maudlin PJ (1994) A constitutive formulation for anisotropic materials suitable for wave propagation computer programs-II. Comput Mech 15(3):201–223. https://doi.org/10.1007/BF00375030

Publisher's Note Springer Nature remains neutral with regard to jurisdictional claims in published maps and institutional affiliations.